IOP Publishing New J. Phys. 27 (2025) 073001 https://doi.org/10.1088/1367-2630/ade736

New Journal of Physics
The open access journal at the forefront of physics

Deutsche Physikalische Gesellschaft DPG
IOP Institute of Physics

Published in partnership with: Deutsche Physikalische Gesellschaft and the Institute of Physics

OPEN ACCESS

RECEIVED
7 March 2025

REVISED
16 May 2025

ACCEPTED FOR PUBLICATION
23 June 2025

PUBLISHED
1 July 2025

PAPER

Reconstruction of single-photon emission with a self-calibrated wQED device based on a transmon qubit

Danilo Labranca[1,2,*], **Adam J Sirois**[1], **Manuel A Castellanos-Beltran**[1], **David I Olaya**[1,3], **Samuel P Benz**[1], **Andrea Giachero**[2,3,4] and **Peter F Hopkins**[1]

[1] RF Technology Division, National Institute of Standards and Technology, Boulder, CO, United States of America
[2] Department of Physics, University of Milano Bicocca, 20126 Milan, Italy
[3] Department of Physics, University of Colorado, Boulder, CO 80309, United States of America
[4] Quantum Sensors Division, National Institute of Standards and Technology, Boulder, CO 80305, United States of America
[*] Author to whom any correspondence should be addressed.

E-mail: danilo.labranca@unimib.it

Keywords: transmon, superconducting qubit, waveguide QED, single-photon source

Abstract

We present a detailed study of a microwave single-photon source utilizing a transmon qubit asymmetrically coupled to two transmission lines: a weakly coupled drive line and a strongly coupled emission line. Our design allows for the generation of single photons in the microwave regime, which are essential for quantum communication, computing, and sensing applications. In addition to single-photon generation, the same design functions as a power sensor and enables precise measurement of the system's attenuation. This dual functionality allows us to calibrate the noise of our amplification chain. This enables a self-calibrated architecture in which the same device acts simultaneously as the photon source and as a reference standard, eliminating the need for external tones or calibrated inputs. With this calibration we reconstruct the density matrix of the emitted photon state, for which we achieve a fidelity of 61.4% and measure a second-order correlation function of $g^{(2)}(0) = 0.06^{+0.45}_{-0.06}$, indicating quantum nature and single-photon characteristics. These results confirm generation of single photons and demonstrate the potential of transmon qubits in advancing quantum technologies in the microwave domain.

1. Introduction

The generation of single-photons has fundamental applications in various quantum technologies, enabling advancements in quantum communication, computing, and sensing. In particular, single-photon sources are key components for quantum key distribution (QKD) protocols [1, 2], quantum networks [3, 4], and quantum sensing systems, where they can serve as calibration tools for single-photon detectors [5, 6]. Significant progress has been achieved in optical single-photon sources using various technologies, including quantum dots, trapped ions, and defect centers in diamond [7–11]. In the microwave frequency range, superconducting circuits containing transmon or flux qubits have been demonstrated as single-photon sources [12–14]. Transmon qubits emerge as a flexible platform to build a single microwave photon source because their strong and tunable coupling to transmission lines allows efficient photon emission, which is critical for single-photon generation in circuit quantum electrodynamics (cQED) and waveguide quantum electrodynamics (wQED) architectures. Waveguide quantum electrodynamics (wQED) describes the interaction of artificial atoms, such as transmon qubits, with photons propagating in one-dimensional transmission lines. This architecture enables strong light-matter interactions, facilitating the realization of on-chip quantum networks and distributed quantum information processing [15–19]. A single-photon source in a wQED system can be used for a variety of applications, including quantum communication over microwave networks and quantum sensing, where single-photon calibration is essential for accurate detector performance.

In this paper, we present measurements of a microwave single-photon source based on a transmon qubit asymmetrically coupled to two transmission lines: a weakly coupled drive line and a strongly coupled emission line. Our design can be easily modified to achieve the desired coupling with the emission line. We quantify the fidelity of single-photon generation and analyze the emitted photon statistics to confirm their quantum nature. A central novelty of this work is the use of Josephson parametric amplifiers (JPAs) to achieve high-efficiency quadrature measurements, combined with a protocol that enables direct, self-calibrated reconstruction of the emitted photon state—without external cancellation tones or calibrated reference sources. The same device is used both as a photon emitter and as a power sensor for absolute calibration of the detection chain. By applying this method to two independent detection channels, we demonstrate and verify the self-calibrating nature of the platform. This dual role represents a key innovation: the device not only emits quantum states, but also serves as its own calibration standard, enabling autonomous, in-situ characterization of quantum microwave signals. We also include a detailed efficiency analysis that supports the consistency between the reconstructed state fidelities and the system's intrinsic performance. These results establish a novel, compact, and autonomous approach for microwave quantum technologies, including quantum communication, single-photon calibration, and sensing.

2. Device characterization

2.1. Measurement setup

The single-photon source is shown in figure 1(a). The chip features a floating transmon with two capacitor pads connected by a dc superconducting quantum interference device (dc-SQUID) for frequency tunability. The qubit is strongly coupled to a port from the upper capacitor pad of the transmon. The lower pad is weakly coupled to a drive line for qubit control. A coplanar waveguide (CPW) terminated by an inductive loop is used to bias the dc-SQUID. The coupling ratio of the two capacitively-coupled ports is designed to prefer emission through the upper port (emission line). The equivalent circuit is shown in figure 1(b) where $C_D \approx 0.21\,\mathrm{fF}$ is the capacitance between the qubit and the drive line, $C_E \approx 3.90\,\mathrm{fF}$ is the capacitance between the emission line and the qubit, and $C_S \approx 87.6\,\mathrm{fF}$ is the effective qubit shunt capacitance. The capacitance values are extracted using finite element electromagnetic simulations. The Josephson junctions in the asymmetric dc-SQUID were designed with critical currents of 85 nA and 52 nA.

The full experimental setup is shown in figure 2. The control pulses for the qubit are generated by an arbitrary waveform generator (AWG) to construct gaussian modulated pulses at intermediate frequency (IF) $\omega_{\mathrm{IF}}/2\pi = 50\,\mathrm{MHz}$, combined by using an IQ-mixer with a gigahertz-frequency local oscillator (LO). The output detection system consists of splitting the emission line with a commercial 90-degree hybrid beam-splitter with wide bandwidth (4 GHz–8 GHz). After the beam-splitter, the two branches (channels) are independently amplified and digitized; each amplifier chain consists of a JPA used in reflection mode, a low-noise high electron mobility transistor (HEMT), and a low-noise room-temperature amplifier (LNA). The amplified signal from each channel is then downconverted by heterodyne detection with IF $\omega_{IF}/2\pi = 50$ MHz by using an image rejecting mixer and then digitized using a digitizer with sampling frequency of $f_s = 500$ MHz.

With this measurement setup we perform a digital, two-quadrature homodyne detection on the signal from each channel following the method described in [20]. The use of a beam-splitter allows us to split the emitted signal into two independent detection paths, each amplified and digitized separately. This configuration enables cross-correlation techniques and independent verification of the reconstructed photon state, which is essential for confirming the self-calibrating nature of the source. However, the presence of the beam-splitter necessarily reduces the detection efficiency in each channel by a factor of approximately two, since the signal is equally divided between the two paths.

2.2. Qubit characterization

The qubit was first characterized using a 2-port vector network analyzer (VNA) to measure the S_{21} scattering parameter through the emission-line monitor/directional coupler and detecting the reflection through one of the two amplified channels after the beam splitter. Figure 3 shows the magnitude of S_{21} as a function of frequency and flux-bias of the dc-SQUID, showing how the qubit transition frequency depends on flux-bias. For all subsequent measurements in this paper, the qubit was operated at the upper sweet-spot of its tunability curve (maximum frequency in figure 3) to minimize flux-noise and match the operating frequency range of the parametric amplifiers.

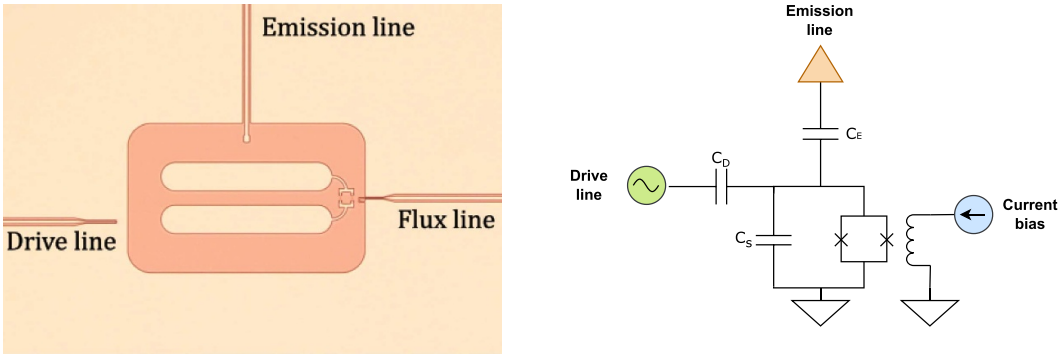

(a) (b)

Figure 1. (a) Picture of the transmon qubit used as a single-photon source. It is a floating transmon with two pads connected by a dc-SQUID to enable tunability. The coupled lines are, clockwise from left: a drive line, weakly coupled to limit photon emission but enable qubit control, an emission line with strong coupling to channel most of the photons through this port, and a flux-line to bias the dc-SQUID. (b) Equivalent circuit scheme: $C_D \approx 0.21\,\text{fF}$, $C_E \approx 3.90\,\text{fF}$, and $C_S \approx 87.6\,\text{fF}$ are the drive-qubit capacitance, the emission-qubit capacitance, and qubit equivalent shunt capacitance, respectively. Due to this asymmetric coupling, we expect that approximately 94% of the generated photons are emitted through the designated output line.

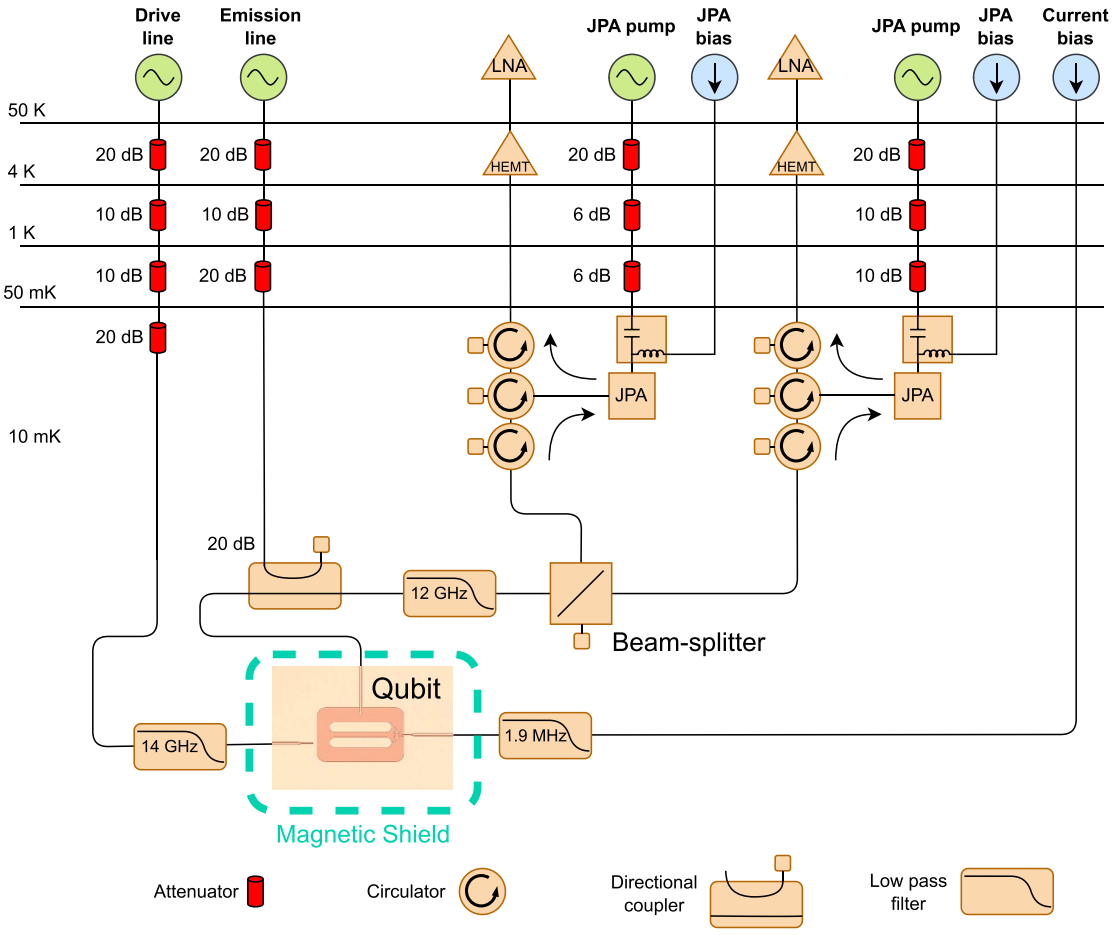

Figure 2. The experimental measurement setup showing the coaxial components at different temperature stages in our dilution refrigerator. The transmon qubit emission line is connected to a beam-splitter and each output channel has an independent amplifier chain (flux pumped JPA in reflection mode + HEMT + LNA). The two JPA pump lines feature different total attenuation, because they have different designs and power requirements. A dedicated drive line is used for qubit control pulses.

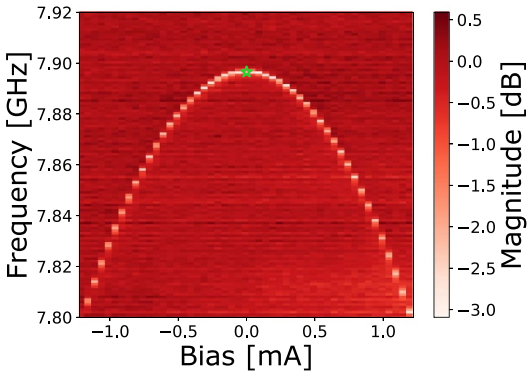

Figure 3. S_{21} measurement showing the transmon frequency dependence on flux bias. The color scale corresponds to the magnitude of S_{21}, which in our setup is equivalent to the magnitude of the reflection coefficient r, as defined in equation (1). The green star represents the frequency used for the measurements in figure 4.

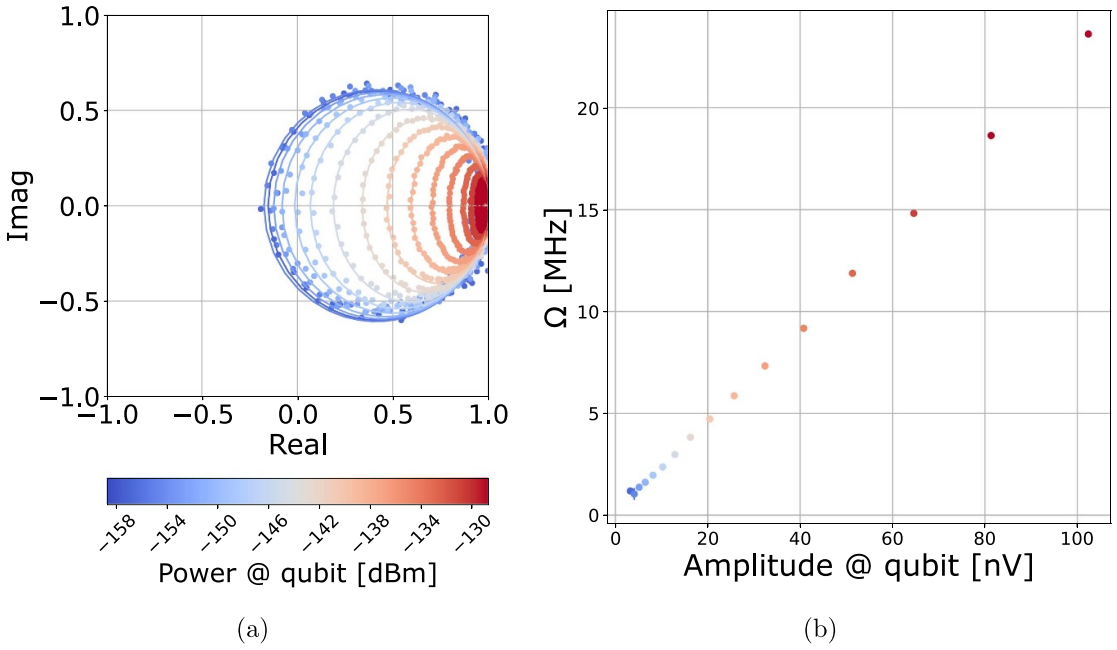

Figure 4. (a) S_{21} resonance circles in the real and imaginary plane measured as a function of excitation power; excitation power is referenced to the qubit, as determined from figure 5. Data are normalized by subtracting the background. The solid lines show the fit performed with shared parameters for all powers. (b) Fits for Rabi frequency Ω as a function of the drive amplitude at the qubit, showing the expected linear dependence. The error bars are smaller than the dots. The color scale applies to both (a) and (b).

By measuring the reflection coefficient, r, at the emission port it is possible to extract the qubit parameters using:

$$r(\Delta) = 1 - \frac{\Gamma_1^r}{\Gamma_2} \frac{1 + i\frac{\Delta}{\Gamma_2}}{1 + \left(\frac{\Delta}{\Gamma_2}\right)^2 + \frac{\Omega^2}{\Gamma_1 \Gamma_2}}, \tag{1}$$

where Δ is the drive-qubit detuning, $\Gamma_1 = \Gamma_1^r + \Gamma_1^{nr}$, Γ_1^r is the qubit relaxation rate due to coupling to the environment through the port, Γ_1^{nr} is the non-radiative relaxation rate, $\Gamma_2 = \Gamma_1/2 + \Gamma_\phi$ and Γ_ϕ is the qubit decoherence rate and Ω is the Rabi frequency [21]. The Rabi frequency is directly related to the power at the qubit coupling port (W_0):

$$W_0 = \frac{\hbar \omega_{01} \Omega^2}{4\Gamma_1^r}, \tag{2}$$

where $\hbar$ is the reduced Planck constant and ω_{01} is the qubit frequency. These expressions are obtained by solving the dynamics of the qubit under a coherent drive as in [21]. Figure 4(a) shows the S_{21} resonance

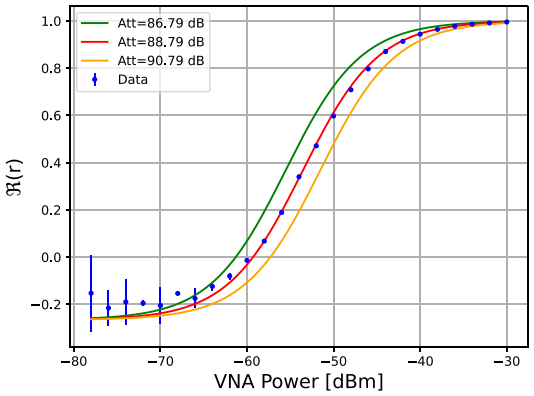

Figure 5. Real part of the reflection coefficient ($\mathcal{R}(r)$) at the emission port as a function of the VNA output power. The data in blue are shown along with the analytical power dependent reflection coefficient from equation (2) for different line attenuation values: in red is the best fitting curve, while in green and orange are the curves with 2 dB less and more attenuation, respectively.

measurement in the real and imaginary plane as a function of the excitation power at the qubit. The data are normalized by subtracting the background measurement with the qubit frequency ω_{01} detuned by several gigahertz using flux bias. At the sweet-spot qubit frequency, we expect the non-radiative losses dominate over pure dephasing, i.e. $\Gamma_1^{nr} \gg \Gamma_\phi$. For the fitting function we therefore assume Γ_ϕ is negligible, which is later confirmed in figure 6(d). To extract the qubit parameters, the data for all powers are fit simultaneously with shared parameters Γ_1 and Γ_1^{nr} and with unique Ω for each power. The best-fit qubit parameters are $\omega_{01}/2\pi = 7.8935$ GHz, $\Gamma_1^r/2\pi = 569.3 \pm 0.3$ kHz and $\Gamma_1^{nr}/2\pi = 339 \pm 3$ kHz, while figure 4(b) shows the Rabi frequency Ω as a function of amplitude.

Using these fit parameters the absolute power [22] at the emission port can be calibrated using equation (2), resulting in (88.79 ± 0.06) dB total attenuation from the VNA output port to the transmon emission port. Figure 5 shows the real part of the reflection coefficient ($\mathcal{R}(r)$) at the emission port as a function of the VNA output power[5]. The data in blue are extracted from the fits in figure 4 and the analytical curves are calculated using equation (2) for different total line attenuation values. In red is the best fitting curve with a total attenuation of 88.79 dB. For reference, the green and orange curves are the cases with 86.79 dB and 90.79 dB total attenuation, respectively.

2.3. Qubit driving and Rabi oscillations

Once the qubit has been characterized, we can drive the qubit through the weakly-coupled port and observe Rabi oscillations. To extract the quadratures X (both I and Q) of the mode that describes the emitted photon at the emission port, we use temporal mode matching:

$$X = \int \mathrm{d}t f(t) X_{\mathrm{out}}(t), \tag{3}$$

where $X_{\mathrm{out}}(t)$ is the continuous quadrature sampled in the experiment and $f(t)$ is the mode matching function. It can be demonstrated that the choice of $f(t)$ that maximizes the efficiency is:

$$f(t) = \sqrt{\Gamma_1} e^{-\frac{\Gamma_1 t}{2}}, \tag{4}$$

where Γ_1 is the qubit relaxation time [23]. We extract the two field quadratures I and Q for each measurement by mode matching the emission field for both channels (1 and 2). We define the complex field detected as:

$$S_j = I_j + iQ_j, \tag{5}$$

where i is the imaginary unit, j indicates the channel, and I and Q are the mode-matched quadratures. If we vary the gaussian pulse width and amplitude we obtain the Rabi oscillations shown in figures 6(a) and (b). Figure 6(b) shows the cross-power measurement that is obtained as $\langle S_2^* S_1 \rangle$ and is a convenient measurement of the photon number operator $\langle a^\dagger a \rangle$, where a is the annihilation operator for the emission mode [24].

[5] Although the VNA power was calibrated at the output port using a commercial power sensor, the measurement at the qubit is an independent, absolute calibration per equation (2).

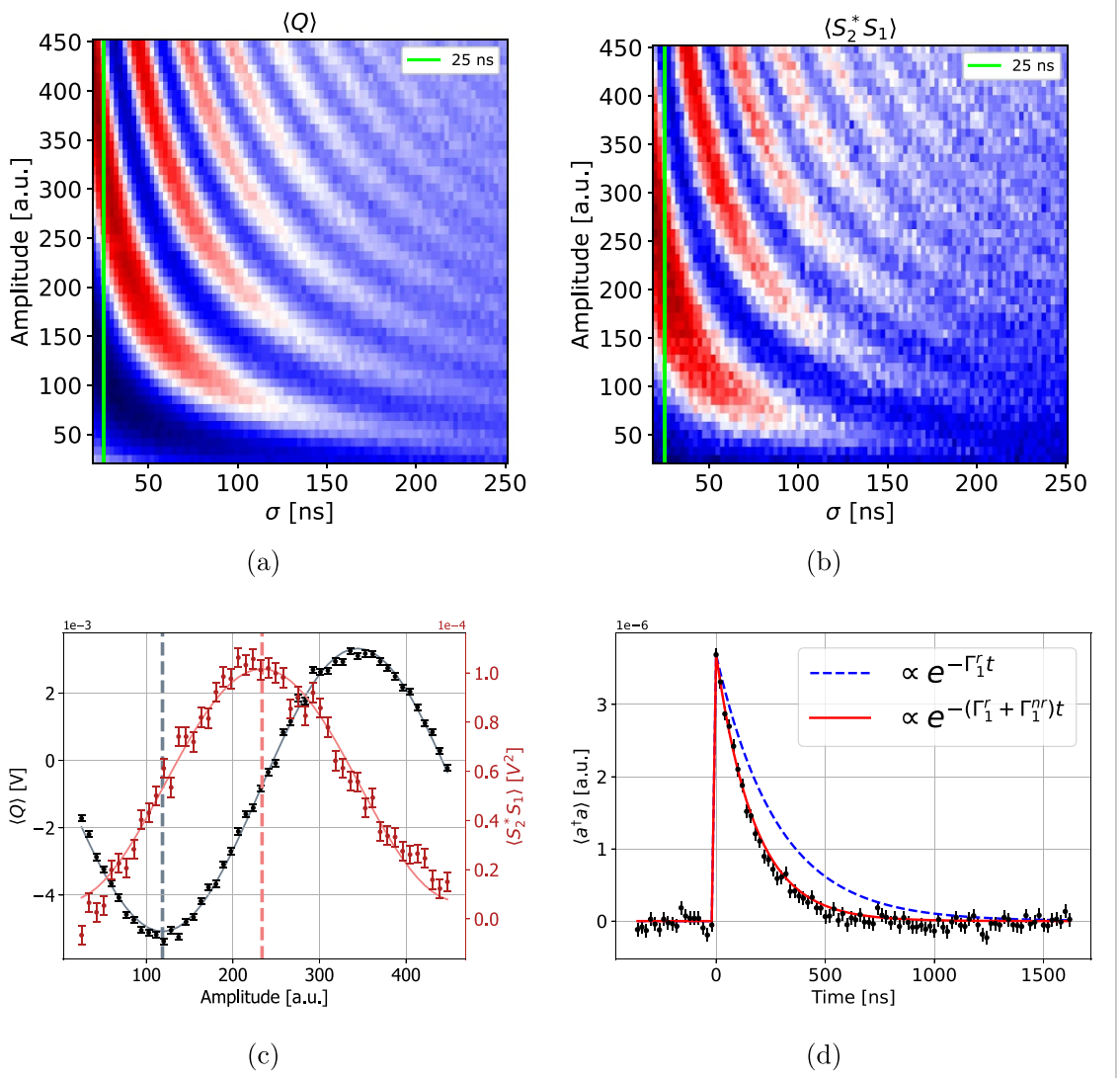

Figure 6. (a) and (b) Rabi oscillations of the transmon qubit obtained by temporal mode matching the emission as function of the gaussian drive pulse σ and amplitude. Both the field quadrature Q ($\propto a$) and the cross-power $\langle S_2^* S_1 \rangle$ ($\propto a^\dagger a$) are shown. In (c) the $\sigma = 25$ ns slices corresponding to the green lines in (a) and (b) are shown for both measurements. In grey and red are the two chosen amplitudes for the $\pi/2$ and π-pulse, respectively. (d) The qubit emission power after driving with a π-pulse. Two exponential curves are shown to emphasize the total qubit decay rate.

Figure 6(c) shows a section of figures 6(a) and (b) that we use to calibrate the π-pulse and $\pi/2$-pulse. The maximum emission in the cross-power corresponds to the emission of a single-photon after a π-pulse and the minimum in Q corresponds to a $\pi/2$-pulse. Figure 6(d) shows the time evolution of the expectation value $\langle a^\dagger a \rangle$ following the application of a π-pulse. This quantity is proportional to the probability of single-photon emission into the output line and reflects the population of the qubit's excited state. The observed exponential decay of $\langle a^\dagger a \rangle$ is governed by the total energy relaxation rate of the qubit, $\Gamma_1 = \Gamma_1^r + \Gamma_1^{nr}$. Two exponential fits are overlaid: one with $\Gamma_1/2\pi = 907.8$ KHz (solid red line), corresponding to the total relaxation rate, and another with $\Gamma_1^r/2\pi = 569.3$ KHz (dashed blue line), corresponding to the radiative component only. The best agreement is found with the total decay rate (red curve), supporting our assumption that non-radiative losses dominate over pure dephasing, i.e. $\Gamma_1^{nr} \gg \Gamma_\phi$. If pure dephasing were significant, the data would lie closer to the blue curve, since Γ_ϕ does not contribute to energy loss and hence to photon emission. The clear preference for the red curve confirms that energy relaxation is the dominant decoherence channel in our system.

3. Density matrix reconstruction

With the control pulses calibrated, next we need to demonstrate that we are indeed generating a single-photon in the emission line. To do so we reconstruct the emitted field density matrix with a Maximum Likelihood Estimation (MLE) method based on moments extraction [23]. In order to properly extract the

density matrix, we first calibrate the total added noise of our amplification chain. The main advantage of this protocol is that the device itself serves as the calibration source without the need for additional experimental changes and measurements. We use data collected from only one output channel in the next section.

3.1. Noise calibration

Using the power calibration described in section 2.2, we estimate the power of a signal at the qubit emission port and therefore the total gain of the system. We measure the peak power $P^{\text{out}}[W]$ (in Watts [W]) at the fridge output with a spectrum analyzer (SA) and compare it with the estimated power $P^{\text{qubit}}[\text{W}]$ at the qubit to obtain the total gain as $G = P^{\text{out}}[\text{W}]/P^{\text{qubit}}[\text{W}]$. By measuring the RMS noise floor $P^{\text{floor}}[\text{W}]$ we can calculate the average number of thermal photons introduced by the detection chain:

$$N_0 = \frac{P^{\text{floor}}[\text{W}]}{GBW\hbar\omega_{01}} - 1 = 4.935 \pm 0.081, \tag{6}$$

where BW is the SA bandwidth. In this treatment N_0 represents the added number of quanta above the vacuum fluctuations $(1/2)$ plus the minimum allowed added noise $(1/2)$. Note that the beam-splitter increases the added noise by a factor of two since we collect in one branch only half of the photons. The corresponding detection efficiency can be calculated as:

$$\eta_{\text{det}} = \frac{1}{1+N_0} = 0.168 \pm 0.003. \tag{7}$$

It is important to note that η_{det} is the detection efficiency of our detection chain and does not include the source efficiency, which we calculate in section 4. The value η_{det} represents the detection efficiency relative to the best achievable efficiency. For $N_0 = 0$, $\eta_{det} = 1$ represents an ideal detection system based on a quantum limited amplifier that adds $\frac{1}{2}$ quanta of noise.

3.2. Data acquisition

We prepare the qubit in three quantum states: $|0\rangle$ (not driving the qubit), $|1\rangle$ (driving with a π-pulse) and $1/\sqrt{2}(|0\rangle + |1\rangle)$ (driving with a $\pi/2$-pulse). We then use temporal mode matching on both quadratures in the same way as the Rabi oscillation measurements from section 2.2 and store each measurement as a pair I_j, Q_j. We measured $N_{\text{meas}} = 2 \times 10^6$ pairs for each state and re-scaled the $I - Q$ values so they match the vacuum state variance of $N_0/2 + 1/2$, where N_0 is known from equation (6) through the self-calibrated measurement. To visualize the field quadrature distribution we construct histograms in the $I - Q$ plane. The results are shown in figures 7(a)–(c). These histograms represent direct measurements of the s-parametrized quasiprobability distributions and they store all the information needed for the density matrix reconstructions. The added noise masks the field quadrature distributions but the profile histogram (figure 7(d)) clearly shows different statistics for the three states. Subtracting the vacuum histogram distribution from the other two emphasizes the actual distribution of the emitted field (figures 7(e) and (f)).

4. Analysis

We now want to find the state that generated these distributions. In our experiments, the density matrix of the microwave field is reconstructed by measuring the normally ordered moments of the field operator $\hat{a}$ up to a fixed order. These moments are extracted from the complex amplitude distribution obtained from repeated measurements of

$$\hat{S} = \hat{a} + \hat{h}^\dagger = \hat{I} + i\hat{Q}, \tag{8}$$

where $\hat{h}$ represents the noise mode of the amplification chain and $\hat{I}$ and $\hat{Q}$ are the two conjugate quadratures of the field. Assuming that the signal and the amplifier noise are uncorrelated, the measured moments of $\hat{S}$ are deconvolved to yield the corresponding moments of $\hat{a}$. The maximum-likelihood estimation is then implemented by minimizing the log-likelihood function

$$\mathcal{L} = -\sum_{n,m}^{n+m\leqslant 8} \frac{1}{\delta_{n,m}^2} \left| \langle (\hat{a}^\dagger)^n \hat{a}^m \rangle_{\text{exp}} - \text{Tr}\left[\rho\, (\hat{a}^\dagger)^n \hat{a}^m\right] \right|^2, \tag{9}$$

where $\langle (\hat{a}^\dagger)^n \hat{a}^m \rangle_{\text{exp}}$ denotes the experimentally determined moments, $\delta_{n,m}$ are the associated standard deviations, and the summation runs over all moments up to the chosen order. The density matrix ρ is estimated subject to the physical constraints $\rho \geqslant 0$ and $\text{Tr}(\rho) = 1$. This approach yields a robust

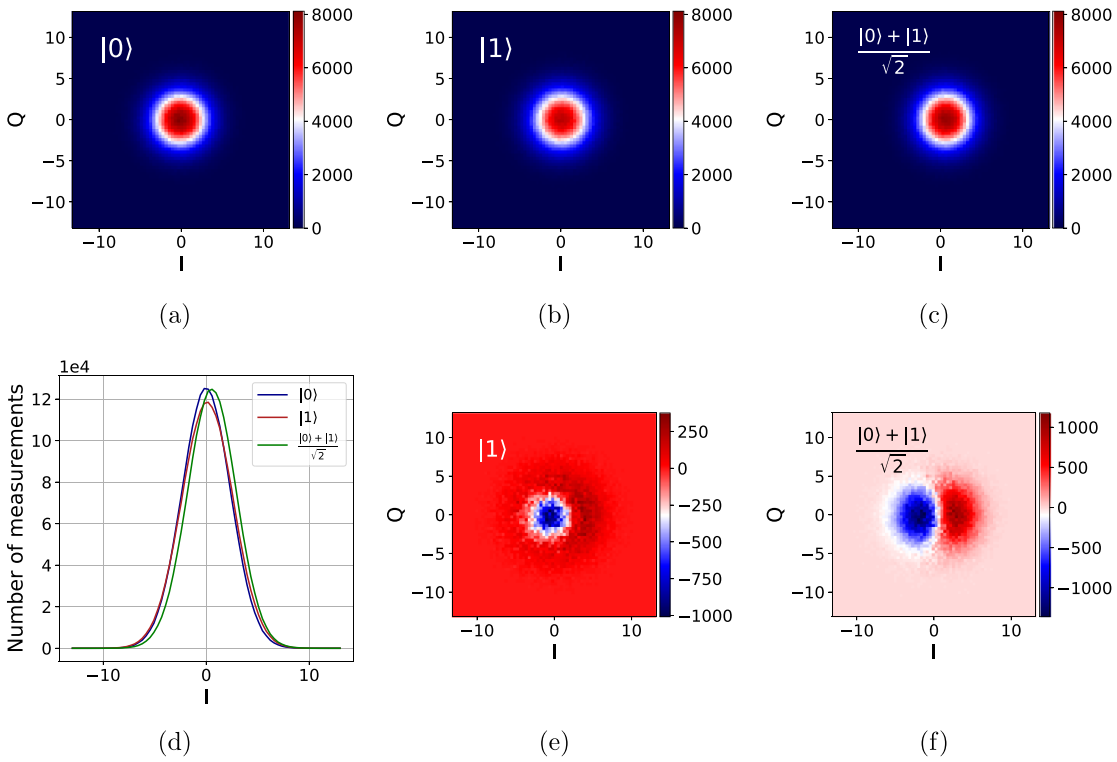

Figure 7. Measured quadrature distributions for the three prepared quantum states: (a) $|0\rangle$, (b) $|1\rangle$, and (c) $\frac{1}{\sqrt{2}}(|0\rangle + |1\rangle)$. (d) Profile distribution for the three states. (e) Resultant quadrature distribution for $|1\rangle$ after subtracting the histogram (a) from (b). (f) Resultant quadrature distribution for $\frac{1}{\sqrt{2}}(|0\rangle + |1\rangle)$ after subtracting the histogram (a) from (c).

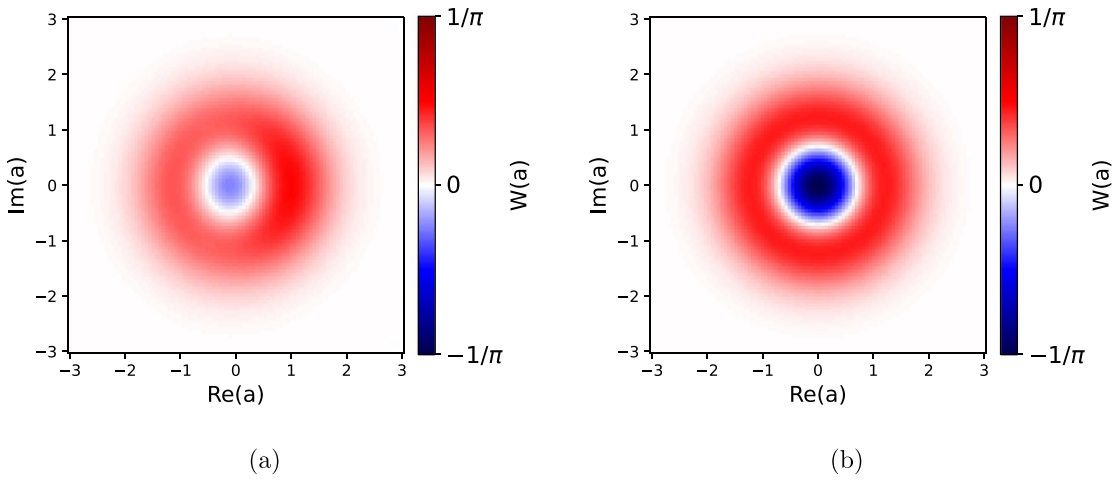

Figure 8. (a) Wigner representation of the reconstructed state emitted by the transmon after a π-pulse. The small circular asymmetry can be explained by an imperfect state preparation creating a coherent mixture of a single photon Fock state with a small amount of vacuum. (b) Wigner representation of a theoretical single-photon Fock state. The a variable represents the reconstructed field as $a = (x + ip)/2$, where x and p are the field quadratures.

reconstruction of the state even in the presence of significant detection noise [23]. We apply this reconstruction methodology to the $|1\rangle$ and $\frac{1}{\sqrt{2}}(|0\rangle + |1\rangle)$ measured quadratures. Figures 8(a), (b), 9(a) and (b) show the Wigner function of the reconstructed density matrices for the two states along with the Wigner functions expected for the prepared state. The negative values of the reconstructed Wigner functions confirm that the generated states are non-classical ($W(0,0) \approx -0.07$ for the $|1\rangle$ state). To quantify our ability of generating the states we calculate the fidelity between the reconstructed (ρ_{reco}) and theoretical

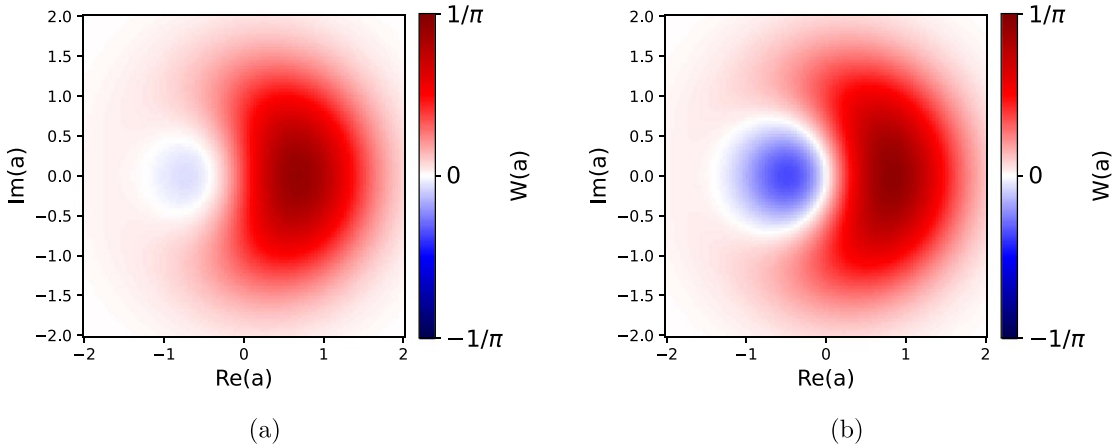

Figure 9. (a) Wigner representation of the reconstructed state emitted by the transmon after a $\pi/2$-pulse. (b) Wigner representation of a theoretical superposition state $|\Psi\rangle = 1/\sqrt{2}(|0\rangle + |1\rangle)$. The a variable represents the reconstructed field variable as $a = (x + ip)/2$, where x and p are the field quadratures.

(ρ_{th}) density matrix

$$\mathcal{F} = \left(\text{Tr}\sqrt{\sqrt{\rho_{\text{reco}}}\,\rho_{\text{th}}\,\sqrt{\rho_{\text{reco}}}}\right)^2. \tag{10}$$

The $|1\rangle$ state is reconstructed with $\mathcal{F} \approx 61.4\%$ and $\frac{1}{\sqrt{2}}(|0\rangle + |1\rangle)$ with $\mathcal{F} \approx 90.3\%$. From the extracted moments we can also calculate the second order correlation function for the single-photon Fock state [25]:

$$g^{(2)}(0) = \frac{\left\langle (a^\dagger)^2 a^2 \right\rangle}{\langle a^\dagger a \rangle^2} = 0.06^{+0.45}_{-0.06}, \tag{11}$$

where the uncertainty is limited by the number of measurements, the value of which is a measurement of the anti-bunching of the emitted photons, showing that the emitted state is indeed non-classical and single-photons are being generated from the source. For an ideal single-photon Fock state, the second-order correlation function at zero time delay is expected to be $g^{(2)}(0) = 0$. This reflects the fundamental property of antibunching: a true single-photon state cannot simultaneously produce two detection events, meaning that two detectors (or the same detector in a time-resolved measurement) will never click at exactly the same time due to a single photon. However, in realistic experimental conditions, various imperfections such as photon losses, background noise, multi-photon contamination, or non-ideal detection efficiencies typically raise the observed value of $g^{(2)}(0)$ above zero. Nevertheless, values substantially below 1 (and particularly values $g^{(2)}(0) < 0.5$) are widely regarded as strong indicators of genuine single-photon emission. In our experiment the observed value of $g^{(2)}(0)$ falls well within this indicative range. Consequently, we interpret this result as robust evidence of single-photon character in the emitted field. The fidelity of reconstruction achieved is mostly limited by the intrinsic source efficiency, which is the efficiency with which the source emits the photon in the wanted direction (i.e. the emission line). The intrinsic efficiency of this source can be estimated as in [26] from Γ_1^r and Γ_2 obtained from the reflection coefficient measurement. Hence the intrinsic efficiency is

$$\eta_{\text{int}} = \frac{\Gamma_1^r}{2\Gamma_2} \approx \frac{\Gamma_1^r}{\Gamma_1^r + \Gamma_1^{nr}} = 0.627 \pm 0.002. \tag{12}$$

The large discrepancy in fidelity between the $|1\rangle$ and $(|0\rangle + |1\rangle)/\sqrt{2}$ states agrees with the expected fidelity of a single-photon source with the measured intrinsic efficiency (η_{int}). The inefficiency can be modeled as a fictitious beam-splitter with transmission $\sqrt{\eta_{\text{int}}}$ and reflection $\sqrt{1-\eta_{\text{int}}}$ (emission in environment). Since the vacuum component $|0\rangle$ remains unaffected by loss, this model implies that only the single-photon component $|1\rangle$ is subject to attenuation, leading to a reduction in the measured coherence and population of states containing $|1\rangle$. As a result, states with larger $|1\rangle$ amplitude (such as the pure $|1\rangle$ state) are more strongly affected by inefficiency than balanced superpositions, thereby explaining the observed discrepancy

in fidelity. In the case of a superposition $|\psi\rangle = \alpha|0\rangle + \beta|1\rangle$ we can calculate the expected fidelity of reconstruction as a function of η_{int}:

$$\mathcal{F}(\alpha, \beta, \eta_{\text{int}}) = |\alpha|^4 + \eta_{\text{int}}|\beta|^4 + (2\sqrt{\eta_{\text{int}}} + 1 - \eta_{\text{int}})\,|\alpha|^2|\beta|^2. \tag{13}$$

Using $\eta_{\text{int}} = 0.627$ the expected fidelities for the $|1\rangle$ and $(|0\rangle + |1\rangle)/\sqrt{2}$ are:

$$\mathcal{F}(\alpha = 0, \beta = 1) = \eta_{\text{int}} \approx 62.7\% \tag{14}$$

$$\mathcal{F}\left(\alpha = \tfrac{1}{\sqrt{2}}, \beta = \tfrac{1}{\sqrt{2}}\right) = \tfrac{1+\sqrt{\eta_{\text{int}}}}{2} \approx 89.6\%. \tag{15}$$

To prove that this intrinsic efficiency is mainly responsible for the reconstruction infidelity, we can include this efficiency in the reconstruction analysis. To do so we must calculate the cumulative efficiency as:

$$\eta_{\text{tot}} = \eta_{\text{int}} \times \eta_{\text{det}} = 0.106 \pm 0.002, \tag{16}$$

corresponding to an average number of thermal photons of

$$N_0^{\text{tot}} = \frac{1}{\eta_{\text{tot}}} - 1 = 8.56 \pm 0.13. \tag{17}$$

Running the reconstruction algorithm on the same data assuming this level of added quanta enhances the reconstructed state fidelity. The resulting reconstruction fidelity increases to $\mathcal{F} \approx 97.3\%$ for the $|1\rangle$ state and to $\mathcal{F} \approx 99.9\%$ for the $\frac{1}{\sqrt{2}}(|0\rangle + |1\rangle)$ state. As a confirmation of the self-calibrated nature of this device, we applied the same analysis to the second branch after the beam-splitter. The noise added by the amplification chain of the second branch is noisier than the first, previously-analyzed branch, presumably due to one or more noisier components in the chain. Using the same calibration and procedure, we measured the number of added quanta and the efficiency of the second branch:

$$N_0^{\text{Branch2}} = 8.40 \pm 0.13 \tag{18}$$

$$\eta^{\text{Branch2}} = 0.106 \pm 0.001 \tag{19}$$

where N_0^{Branch2} is the added number of quanta for the second branch not accounting for the intrinsic efficiency. The fidelity of reconstruction of the density matrix for this branch is compatible with the previous results: $\mathcal{F}^{\text{Branch2}} \approx 61.3\%$ for the $|1\rangle$ state and $\mathcal{F}^{\text{Branch2}} \approx 85.6\%$ for the $\frac{1}{\sqrt{2}}(|0\rangle + |1\rangle)$ state. If we account for the intrinsic inefficiency of the source the total number of added quanta is:

$$\left(N_0^{\text{Branch2}}\right)^{\text{tot}} = 14.00 \pm 0.20 \tag{20}$$

$$\left(\eta^{\text{Branch2}}\right)^{\text{tot}} = 0.055 \pm 0.001. \tag{21}$$

The reconstructed MLE density matrices reached $\mathcal{F}^{\text{Branch2}} \approx 98.1\%$ for the $|1\rangle$ state and $\mathcal{F}^{\text{Branch2}} \approx 93.4\%$ for the $\frac{1}{\sqrt{2}}(|0\rangle + |1\rangle)$ state. These results confirm that the limiting factor to the reconstruction fidelity is the generation efficiency of the source. Each time the qubit is excited, the corresponding emission can occur through the emission port (approximately 63% of the time) or through any other non-radiative channel that we are unable to detect. The limited generation efficiency is mostly related to the ratio between the emission port coupling Γ_1^r and the non-radiative couplings Γ_1^{nr}. Increasing the coupling Γ_1^r by a factor of 5 is achievable with a simple redesign, for example by reducing the distance between the emission line and the transmon pad, leading to an intrinsic efficiency $\eta_{\text{int}} \approx 90\%$ improvement with similar non-radiative losses. A relatively small coupling Γ_1^r was chosen to obtain a qubit $T_1 \approx 100$ ns to be able to use control pulses on the scale of tens of nanoseconds. Stronger coupling rates would result in a reduced energy relaxation time T_1, requiring high-speed control electronics capable of producing sub-10 ns pulses to operate this device. These electronics are available but, due to spectrum broadening from the faster pulses, would lead to significant rates of state leakage if no modifications were made to increase qubit anharmonicity and improve the pulse spectrum, such as using DRAG pulses [27]. The high value of Γ_1^r from the increased qubit/transmission line coupling provides sufficient design space to increase the transmon anharmonicity by lowering the E_j/E_c ratio; the resultant increase in qubit decoherence due to increased charge noise sensitivity can be tolerated without significantly degrading the device efficiency. Simulations of the redesigned transmon-based device, featuring a 5X-stronger coupling, suggest that an anharmonicity of approximately 450 MHz (previously $\sim$

220 MHz) can be achieved with $E_J/E_C \approx 43$ (with $f_{01} \approx 7.9$ GHz); under these conditions, the pure dephasing time T_ϕ, limited by charge noise, remains significantly longer than the relaxation time T_1, which is expected to be around 10 ns [28]. In contrast, targeting similar anharmonicities at lower frequencies $f_{01} \lesssim 5.5$ GHz may not be feasible. This would require operating at smaller E_J/E_C ratios, entering a regime where T_ϕ is predicted to become too strongly limited by increased sensitivity to offset charge fluctuations [28]. Higher anharmonicities can be achieved with alternative designs such as fluxonium qubits [29]. Future designs can be modified with the specific application of the source in mind.

5. Conclusions

This paper demonstrates a microwave single-photon source based on a transmon qubit asymmetrically coupled to two transmission lines. We show a complete analysis of an itinerant microwave photon state reconstruction and highlight the different contributions to the source and detection efficiencies. In addition to our device's role as a single-photon source, the same design was demonstrated as a power sensor and was used to measure the attenuation of the system, showcasing its versatility in advancing quantum technologies. The design's calibration capability enabled the reconstructions of different emitted photon states, achieving fidelities of 90.3% for a superposition state and 61.4% for the $|1\rangle$ state, with a second-order correlation function ($g^{(2)}(0) = 0.06^{+0.45}_{-0.06}$) confirming its single-photon nature. These reconstruction fidelities are in good agreement with the expected values based on the intrinsic and independently calibrated detection efficiencies, providing evidence for the quantitative reliability of the self-calibrated protocol. This work experimentally demonstrates that the same physical device can provide both absolute power calibration and single-photon generation. Using the transmon as an internal power reference, we extracted the total system attenuation and gain, and independently quantified the added noise of the amplification chain. These calibrated parameters enabled a self-consistent reconstruction of the emitted quantum states without the use of external references. Moreover, the agreement between the independently reconstructed density matrices from two separate detection channels further confirmed the internal consistency and self-calibrating nature of the platform.

The main limitations in fidelity are due to intrinsic source efficiency (63%). For practical applications, where high-precision state preparation is essential, the objective is to achieve fidelities approaching 100%. Enhancing the coupling design and improving detection methods could significantly increase performance; intrinsic efficiencies up to 90% are feasible [26]. This performance is competitive with state-of-the-art single-photon sources based on quantum dots, which have demonstrated internal efficiencies exceeding 90% [30]. This study demonstrates the potential of transmon-based designs for generating single photons at microwave frequencies, with practical applications in quantum communication and sensing. Future work can focus on improving the source efficiency and the emission rate for specific applications.

Data availability statement

The data that support the findings of this study are openly available at the following URL/DOI: https://board.unimib.it/datasets/vzs49gddsm/1.

Acknowledgments

We acknowledge the NIST Advanced Microwave Photonics Group for providing the JPAs. We thank Thomas Gerrits and Leonardo Banchi for their valuable comments and insightful discussions. We also thank Scott Glancy for his guidance and the helpful discussions on quantum state reconstruction techniques. This work is partially supported by the Italian National Quantum Science and Technology Institute (PNRR MUR Project PE0000023-NQSTI) by the Italian National Centre for HPC Big Data and Quantum Computing (PNRR MUR Project CN0000013-ICSC). AG acknowledges support by the Horizon 2020 Marie Skłodowska-Curie actions (H2020-MSCA-IF GA No.101027746).

References

[1] Zahidy M *et al* 2024 Quantum key distribution using deterministic single-photon sources over a field-installed fibre link *npj Quantum Inf.* **10** 2
[2] Yang J *et al* 2024 High-rate intercity quantum key distribution with a semiconductor single-photon source *Light Sci. Appl.* **13** 150
[3] Couteau C, Barz S, Durt T, Gerrits T, Huwer J, Prevedel R, Rarity J, Shields A and Weihs G 2023 Applications of single photons to quantum communication and computing *Nat. Rev. Phys.* **5** 326–38
[4] Gao T, von Helversen M, Antón-Solanas C, Schneider C and Heindel T 2023 Atomically-thin single-photon sources for quantum communication *npj 2D Mater. Appl.* **7** 4

[5] Braggio C et al 2024 Quantum-enhanced sensing of axion dark matter with a transmon-based single microwave photon counter (arXiv:2403.02321)
[6] Besse J-C, Gasparinetti S, Collodo M C, Walter T, Kurpiers P, Pechal M, Eichler C and Wallraff A 2018 Single-shot quantum nondemolition detection of individual itinerant microwave photons *Phys. Rev. X* **8** 021003
[7] Keller M, Lange B, Hayasaka K, Lange W and Walther H 2004 Continuous generation of single photons with controlled waveform in an ion-trap cavity system *Nature* **431** 1075–8
[8] Kurtsiefer C, Mayer S, Zarda P and Weinfurter H 2000 Stable solid-state source of single photons *Phys. Rev. Lett.* **85** 290
[9] Lounis B and Moerner W E 2000 Single photons on demand from a single molecule at room temperature *Nature* **407** 491–3
[10] Georgieva H et al 2024 Disseminable single-photon source for quantum radiometry *Appl. Phys. Lett.* **125** 264002
[11] Schmunk W et al 2012 Photon number statistics of NV centre emission *Metrologia* **49** S156–60
[12] Houck A A et al 2007 Generating single microwave photons in a circuit *Nature* **449** 328–31
[13] Peng Z, De Graaf S, Tsai J and Astafiev O 2016 Tuneable on-demand single-photon source in the microwave range *Nat. Commun.* **7** 12588
[14] Zhou Y, Peng Z, Horiuchi Y, Astafiev O and Tsai J 2019 Efficient tunable microwave single-photon source based on transmon qubit *2019 IEEE Int. Superconductive Electronics Conf. (ISEC)* (IEEE) pp 1–3
[15] Sheremet A S, Petrov M I, Iorsh I V, Poshakinskiy A V and Poddubny A N 2023 Waveguide quantum electrodynamics: collective radiance and photon-photon correlations *Rev. Mod. Phys.* **95** 015002
[16] Kolchin P, Oulton R F and Zhang X 2011 Nonlinear quantum optics in a waveguide: distinct single photons strongly interacting at the single atom level *Phys. Rev. Lett.* **106** 11
[17] Kannan B et al 2020 Waveguide quantum electrodynamics with superconducting artificial giant atoms *Nature* **583** 775–9
[18] Chuikin O A, Greenberg Y S, Shtygashev A A and Moiseev A G 2024 Single-photon stimulated emission in waveguide quantum electrodynamics *Eur. Phys. J. B* **97** 159
[19] Yin X-L, Liu Y-H, Huang J-F and Liao J-Q 2022 Single-photon scattering in a giant-molecule waveguide-QED system *Phys. Rev. A* **106** 013715
[20] Lang C 2014 Quantum microwave radiation and its interference characterized by correlation function measurements in circuit quantum electrodynamics *PhD Dissertation* (available at: https://api.semanticscholar.org/CorpusID:125166829)
[21] Lu Y et al 2021 Characterizing decoherence rates of a superconducting qubit by direct microwave scattering *npj Quantum Inf.* **7** 35
[22] Hönigl-Decrinis T, Shaikhaidarov R, de Graaf S E, Antonov V N and Astafiev O V 2020 Two-level system as a quantum sensor for absolute calibration of power *Phys. Rev. A* **13** 024066
[23] Eichler C, Bozyigit D and Wallraff A 2012 Characterizing quantum microwave radiation and its entanglement with superconducting qubits using linear detectors *Phys. Rev. A* **86** 032106
[24] Zhou Y, Peng Z, Horiuchi Y, Astafiev O and Tsai J 2020 Tunable microwave single-photon source based on transmon qubit with high efficiency *Phys. Rev. Appl.* **13** 034007
[25] Leonhardt U and Paul H 1995 Measuring the quantum state of light *Prog. Quantum Electron.* **19** 89–130
[26] Lu Y, Bengtsson A, Burnett J J, Suri B, Sathyamoorthy S R, Nilsson H R, Scigliuzzo M, Bylander J, Johansson G and Delsing P 2021 Quantum efficiency, purity and stability of a tunable, narrowband microwave single-photon source *npj Quantum Inf.* **7** 140
[27] Chow J M, DiCarlo L, Gambetta J M, Motzoi F, Frunzio L, Girvin S M and Schoelkopf R J 2010 Optimized driving of superconducting artificial atoms for improved single-qubit gates *Phys. Rev. A* **82** 040305(R)
[28] Koch J, Yu T M, Gambetta J, Houck A A, Schuster D I, Majer J, Blais A, Devoret M H, Girvin S M and Schoelkopf R J 2007 Charge-insensitive qubit design derived from the cooper pair box *Phys. Rev. A* **76** 042319
[29] Manucharyan V E, Koch J, Glazman L I and Devoret M H 2009 Fluxonium: single cooper-pair circuit free of charge offsets *Science* **326** 113–6
[30] Dlaka D, Androvitsaneas P, Young A, Ma Q, Harbord E and Oulton R 2024 Design principles for >90% efficiency and >99% indistinguishability broadband quantum dot cavities *New J. Phys.* **26** 093022